NJC

ROYAL SOCIETY OF CHEMISTRY

PAPER

View Article Online
View Journal | View Issue

Cite this: *New J. Chem.*, 2020, 44, 2452

A procalcitonin photoelectrochemical immunosensor: NCQDs and Sb_2S_3 co-sensitized hydrangea-shaped WO_3 as a matrix through a layer-by-layer assembly†

Xin Liu,[ab] Chunzhu Bao,[ab] Xinrong Shao,[ab] Yong Zhang,[ab] Nuo Zhang,[ab] Xu Sun,[ab] Dawei Fan,*[ab] Qin Wei[ab] and Huangxian Ju[abc]

Received 10th December 2019,
Accepted 9th January 2020

DOI: 10.1039/c9nj06118e

rsc.li/njc

Using nitrogen-doped carbon quantum dots (NCQDs) and antimony trisulfide (Sb_2S_3) to co-sensitize hydrangea-shaped tungsten trioxide (WO_3), a novel photoelectrochemical (PEC) immunosensor was constructed to sensitively detect procalcitonin (PCT). WO_3 possessed a three-dimensional structure with uniform size and large surface area on the indium tin oxide (ITO) electrode. NCQDs with abundant carboxy groups and excitation-independent PEC behavior were modified on the surface of the WO_3 coating to enhance photochemical activity. Hence, the hydrangea-shaped WO_3/NCQDs/Sb_2S_3 composite was obtained by modifying NCQDs and well-crystallized Sb_2S_3 nanoparticles on WO_3 through a layer-by-layer assembly. It is worth noting that the photoelectric signal of WO_3/NCQDs/Sb_2S_3 was about 8 times that of pure WO_3 under visible light excitation. Moreover, the PEC immunosensor showed a large-scale response (0.001–100 ng mL^{-1}) and a low detection limit (0.42 pg mL^{-1}) under the best experimental conditions. This PEC immunosensor has advantages such as simplicity, facile fabrication, high sensitivity and strong stability, which have good research value in the analysis and detection of disease biomarkers.

1. Introduction

The photoelectrochemical (PEC) immunosensor is a new analytical method based on the PEC process and chemical or biological probe recognition.[1–3] Using visible light as an excitation signal and photocurrent as a detection signal, the PEC immunosensor owns many advantages such as higher sensitivity, low background signals, low cost and inherent miniaturization. It has broad application prospect in biological and chemical analyses.[4–8]

In recent years, due to the electrochemical behavior and photoelectric conversion of new semiconductor electrode and electrolyte solution systems under visible light, the research on semiconductor photoelectric chemistry has received extensive attention.[9–11] N-Type semiconductors have exciting properties of various types and were easy to synthesize and modify. Besides, the photoanode electron is the main carrier, and the photocurrent response is enhanced when the electron donor (AA) is oxidized by a hole. Hence, n-type semiconductors with a high valence band are good for photoanode.[12] Tungsten oxide (WO_3), an n-type semiconductor, possesses a high valence band position and a suitable band gap (~2.6 eV). WO_3 has advantages of good chemical stability, diverse morphology and low cost, which has been widely used in the field of photoelectrocatalysis.[13–15] In this work, we synthesized hydrangea-shaped WO_3 based on the method reported in the literature.[16] The WO_3 has a large specific surface area, which is advantageous to load nanoparticles with high PEC properties on its surface. In addition, carbon quantum dots (CQDs) have been extensively researched due to their characteristic features such as appropriate size, good biocompatibility and strong reservoir capacity.[17,18] In particular, CQDs have wide applications in electrochemical luminescence and other exclusive fields.[19] However, compared with pure CQDs, nitrogen-doped carbon quantum dots (NCQDs) have raised concerns due to their better water solubility and electron transport capacity.[20–23] Currently, extensive research on NCQDs/TiO_2,[24] NCQDs/SnO_2,[25] $BiVO_4$/NCQDs/Ag_3PO_4[26] and other composite materials showed that the combination of NCQDs and semiconductor materials could enhance the photoelectric

[a] *Collaborative Innovation Center for Green Chemical Manufacturing and Accurate Detection, School of Chemistry and Chemical Engineering, University of Jinan, Jinan 250022, P. R. China. E-mail: jndxfandawei@126.com; Tel: +86-531-82760510*

[b] *Key Laboratory of Interfacial Reaction & Sensing Analysis in Universities of Shandong, School of Chemistry and Chemical Engineering, University of Jinan, Jinan 250022, P. R. China*

[c] *Key Laboratory of Analytical Chemistry for Life Science, School of Chemistry and Chemical Engineering, Nanjing University, Nanjing 210023, P. R. China*

† Electronic supplementary information (ESI) available. See DOI: 10.1039/c9nj06118e

activity. Herein, in our work, the NCQDs were combined with WO_3 to obtain WO_3/NCQD composites successfully.

Besides, selecting and preparing excellent semiconductor materials have been a research hotspot in the field of photoelectric chemistry.[27–31] Sb_2S_3, a direct band gap nanoparticle (about 2.0 eV), shows strong absorption ability in the visible region.[32] Moreover, Sb_2S_3 has low toxicity and high stability, which made it a very promising absorbent for next-generation photovoltaics.[33,34] In this experiment, to obtain a highly efficient PEC immunosensor substrate, Sb_2S_3 with high quality and high surface coverage was combined on the WO_3/NCQD composite to form the WO_3/NCQDs/Sb_2S_3 composite with strong photoelectric activity.

Procalcitonin (PCT) is a protein that was elevated in plasma during severe bacterial and parasitic infections as well as sepsis and multiple organ failure.[35–37] Therefore, it could be used as an acute parameter to distinguish the diagnosis of bacterial and non-bacterial inflammation.[38] Herein, it was first reported that PCT was selected as our detection object to study the behavior of NCQDs and Sb_2S_3 co-sensitized hydrangea-shaped WO_3 PEC immunosensors. Therefore, a novel and ultrasensitive PEC immunosensor based on WO_3/NCQDs/Sb_2S_3 composites was prepared for the detection of PCT.

2. Experimental section

2.1. Experimental reagents and apparatus

Sodium tungstate dehydrate ($Na_2WO_4{\cdot}2H_2O$) and oxalic acid ($H_2C_2O_4$) were purchased from Kermel Chemical Reagent Co. Ltd (Tianjin, China). Antimonous chloride ($SbCl_3$) and sodium sulfide (Na_2S) were purchased from Sinopharm Chemical Reagent Co. Ltd (Beijing, China). Tri(hydroxymethyl)aminomethane ($C_4H_{11}NO_3$) was provided by Shanghai Haohong biopharmaceutical technology Co. Ltd (Shanghai, China). The other reagents were obtained from the ESI.†

The CHI760E electrochemical workstation (Shanghai, China) was used for PEC measurement. X-ray diffraction (XRD) was performed using a D8 advance X-ray diffractometer (Bruker AXS, Germany). Fourier transform infrared (FT-IR) spectra were recorded using a Shimadzu VERTEX 70 spectrometer. The other details for the measurement can be offered in ESI.†

2.2. Preparation of hydrangea-shaped WO_3 and NCQDs

A hydrothermal synthesis method was adopted to synthesize hydrangea-shaped WO_3.[16] First, 11 mmol $Na_2WO_4{\cdot}2H_2O$ was dissolved in ultrapure water (20 mL) under magnetic agitation. A HCl solution (6 mol L^{-1}) was added to the obtained liquid drop by drop, keeping the pH value at 1.5, and then NaCl (22 mmol) and $H_2C_2O_4$ (11 mmol) were added to the above mixture. After stirring for 30 min, another 50 mL of ultrapure water was added. Soon after, the resulting liquid was moved into a 100 mL Teflon-lined stainless steel autoclave (150 °C) for 1 h. The precipitation was naturally cooled and then washed with ultrapure water and ethanol, respectively. The obtained precipitation was dried in vacuum for further use.

NCQDs were prepared according to a procedure previously reported in the literature.[39] First, 2 g of diethylenetriaminepentaacetic acid (DTPA) was placed in ultrapure water (20 mL) under magnetic stirring. The suspension was heated (<250 °C) to a colorless solution. Upon continuous heating, a yellow solid appeared and dissolved in ultrapure water (20 mL). Excess DTPA was removed by centrifugation (8000 rpm, 15 min), and the liquid supernatant was freeze-dried to get NCQDs.

2.3. Preparation of buffer solution Tris–HCl (pH 8.5)

Briefly, 1.21 g of tri(hydroxymethyl)aminomethane ($C_4H_{11}NO_3$) was dissolved in 1 L of ultrapure water (solution A), and 0.5 mL of hydrochloric acid (65%) was added to 5 mL ultrapure water (solution B). The buffer solution Tris–HCl (pH 8.5) was obtained by adding solution B to solution A drop by drop.

2.4. Construction of PEC immunosensors

The ITO electrode was chopped into pieces of 2.5 × 0.8 cm^2 dimension, which were cleaned with a series of solutions (aqueous solution of detergent, acetone, anhydrous ethanol and ultrapure water), and dried (70 °C) for later use. The construction process of the PEC immunosensor was studied in Scheme 1. Briefly, 4 mg mL^{-1} WO_3 (10 μL) dispersion liquid was coated onto an ITO electrode, dried and then calcinated (300 °C) for 180 min. Then, 1 mol L^{-1} NCQD solution (8 μL) was modified on an ITO/WO_3 electrode for 30 min and the excess NCQDs were washed off to obtain an ITO/WO_3/NCQD electrode. Soon after, 0.06 mol L^{-1} $SbCl_3$ ethanol solution (4 μL) and 0.1 mol L^{-1} Na_2S aqueous solution (4 μL) were successively modified onto the above electrode for 30 min, and then, washed and dried at room temperature to get an ITO/WO_3/NCQDs/Sb_2S_3 electrode. Subsequently, dopamine (DA) was dissolved in a Tris–HCl (pH 8.5) solution to obtain a solution with concentration of 0.1 mol L^{-1}, and 4 μL of this solution was then modified onto the above electrode and naturally dried. After DA self-polymerized to PDA, the ultrapure water was used to remove the excess DA. Subsequently, 4 μL of 1 μg mL^{-1} anti-PCT, 4 μL of 1 mg mL^{-1} BSA aqueous solution, and 4 μL of PCT

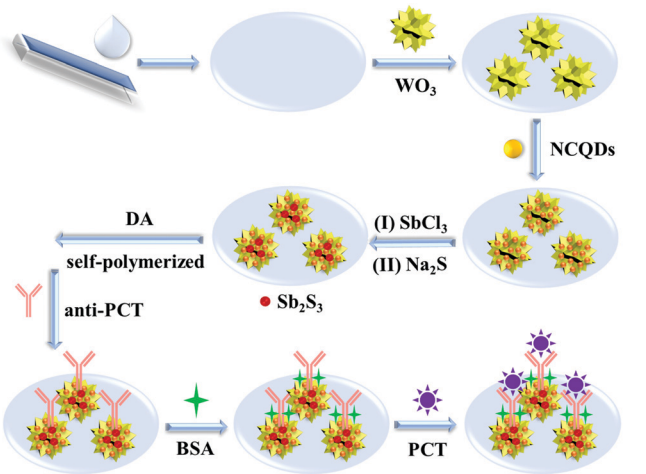

Scheme 1 Construction process of the PEC immunosensor.

with different concentrations were successively dropped onto the above electrodes. All of them need to be washed with water during this process. Hence, the ITO/WO_3/NCQDs/Sb_2S_3/PDA/anti-PCT/BSA/PCT electrodes were obtained.

3. Results and discussion

3.1. Characteristic description of WO_3, NCQDs, Sb_2S_3, WO_3/NCQDs and WO_3/NCQDs/Sb_2S_3

Scanning electron microscopy (SEM) and energy-dispersive spectroscopy (EDS) were used to analyze the elemental composition and morphologies of the prepared materials, respectively. A mass of nanosheets self-assembled together to form hydrangea-shaped WO_3 (Fig. 1A). The three-dimensional structure of hydrangea possesses a uniform size and large surface area, which was conducive to the loading of nanoparticles with excellent performance. With the sequential coating of NCQDs and Sb_2S_3, the laminates of the materials on the electrode gradually became thicker (Fig. 1B and C). The TEM image (Fig. S1A, ESI†) demonstrated that NCQDs were small in size of nearly spherical morphology, which was beneficial to combination with hydrangea-shaped WO_3. As shown in Fig. 1C, Sb_2S_3 exhibits irregular aggregation morphology with rough surface. Moreover, Sb_2S_3 nanoparticles successfully bound on the surface of WO_3/NCQDs to obtain WO_3/NCQDs/Sb_2S_3 composites. Fig. 1D represents the TEM image of WO_3/NCQDs/Sb_2S_3 composites. From Fig. 1E–I, no mapping image of carbon element was given because it was tested on a carbon-sprayed copper screen. W and O elements were assigned to WO_3, element N could be ascribed to NCQDs, and elements Sb and S were from Sb_2S_3. The uniform distribution and highly overlapped elements proved that NCQDs and Sb_2S_3 were successfully combined with WO_3. Besides, the EDS image (Fig. S1B, ESI†) also contained elements W, O, N, C, Sb and S, which further confirmed the hydrangea-shaped WO_3/NCQDs/Sb_2S_3 composite was prepared successfully.

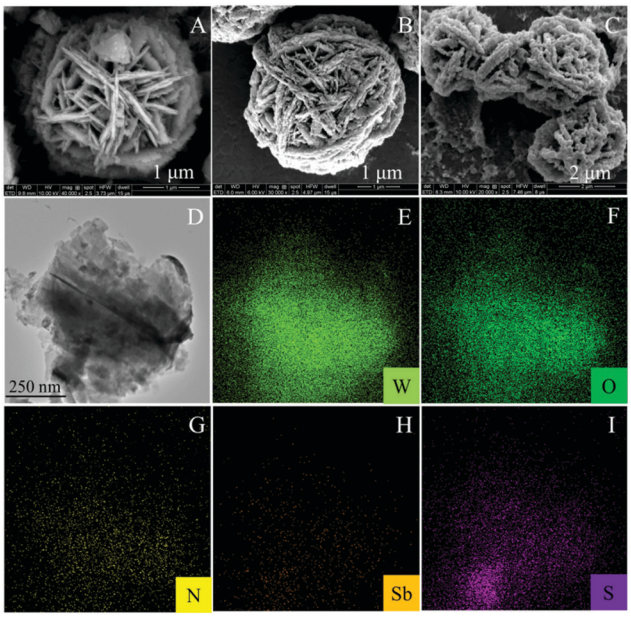

Fig. 1 SEM images of hydrangea-shaped WO_3 (A), WO_3/NCQDs (B), and WO_3/NCQDs/Sb_2S_3 (C), TEM image of WO_3/NCQDs/Sb_2S_3 (D) and the corresponding element mapping images of W (E), O (F), N (G), Sb (H) and S (I).

Fig. 2A and B shows the X-ray diffraction (XRD) patterns of the prepared materials. The curve of WO_3 confirmed that hydrangea-shaped WO_3 was a mixture which with different crystal types included monoclinic WO_3 (PDF #84-0886), cubic $WO_3 \cdot H_2O$ (PDF #41-0905) and hexagonal WO_3 (PDF #33-1387).[16] As the concentration of NCQDs was lower in WO_3/NCQDs and WO_3/NCQDs/Sb_2S_3 composites, the peak of NCQDs was difficult to observe. Moreover, NCQDs was used as the linker between WO_3 and Sb_2S_3 materials. The modification of NCQDs could be proved in further experiments. Besides, the XRD peaks of Sb_2S_3 were indexed to PDF #42-1393, and the XRD peaks of Sb_2S_3 (Fig. 2B) were also found in the WO_3/NCQDs/Sb_2S_3 composite.[40,41]

Fig. 2C shows the UV-vis diffuse reflectance spectra of WO_3 (curve a), WO_3/NCQDs (curve b) and WO_3/NCQDs/Sb_2S_3 (curve c). In the visible light region, the absorption wavelength of hydrangea-shaped WO_3 was shorter than 500 nm, so that the visible light utilization efficiency of WO_3 was low. The absorption range of WO_3/NCQDs was increased by NCQD modification. Besides, WO_3/NCQDs/Sb_2S_3 composites had strong absorption ability in the whole region, which indicated that the WO_3/NCQDs/Sb_2S_3 composite could significantly improve the utilization efficiency of visible light.

The Fourier transform infrared (FT-IR) spectra (Fig. 2E) of WO_3 (curve a), NCQDs (curve b), Sb_2S_3 (curve c) and WO_3/NCQDs/Sb_2S_3 (curve d) were studied. From curve a, it can be observed that the wide peak belonged to the stretching vibration of W–O–W bond ($\sim$817 cm^{-1}). In addition, the strong sharp peak was the W–OH stretching vibration ($\sim$1398 cm^{-1}), it was because water molecules adsorbed onto the surface of WO_3.[42] From curve b, it can be observed that the absorption band (1734 cm^{-1}, 1385 cm^{-1}) belonged to the stretching vibration of C=O and bending vibration of C–O respectively. The stretching property of carbon-nitrogen bond was revealed by the peak of 1221 cm^{-1}. The abundant –COOH on NCQD surface facilitated their stability and hydrophilicity. The absorption peaks at 400–700 cm^{-1} were attributed to the presence of orthorhombic crystal structure of Sb_2S_3 (curve c).[43,44] Besides, the FT-IR spectra of WO_3/NCQDs/Sb_2S_3 composites showed the characteristic peaks of WO_3, NCQDs and Sb_2S_3.

3.2. Characterization of the construction of PEC immunosensors

The photocurrent–time graph during a layer-by-layer assembly of the PEC immunosensor is shown in Fig. 3A. AA as the ideal electron donor inhibited the binding of e^-/h^+, so as to obtain a good and stable PEC signal. The uncovered ITO electrode (curve a) showed extremely weak photocurrent to visible light, almost 0 μA. The electrode had a particular response and improved the photocurrent signal when WO_3 was coated onto the electrode (curve b). Subsequently, NCQDs (curve c) were modified onto WO_3, and then the photocurrent increased.

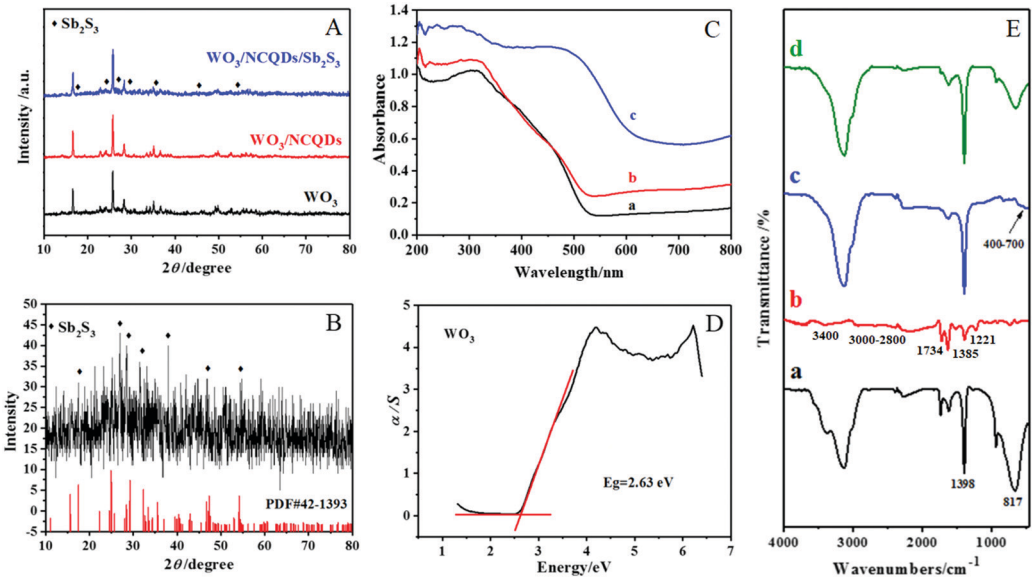

Fig. 2 (A) XRD patterns of WO_3, WO_3/NCQDs, and WO_3/NCQDs/Sb_2S_3 and (B) pure Sb_2S_3. (C) UV-vis diffuse reflectance spectra of (a) WO_3, (b) WO_3/NCQDs, (c) and WO_3/NCQDs/Sb_2S_3. (D) The band gap energy spectra of WO_3. (E) FT-IR spectra of (a) WO_3, (b) NCQDs, (c) Sb_2S_3, and (d) WO_3/NCQDs/Sb_2S_3.

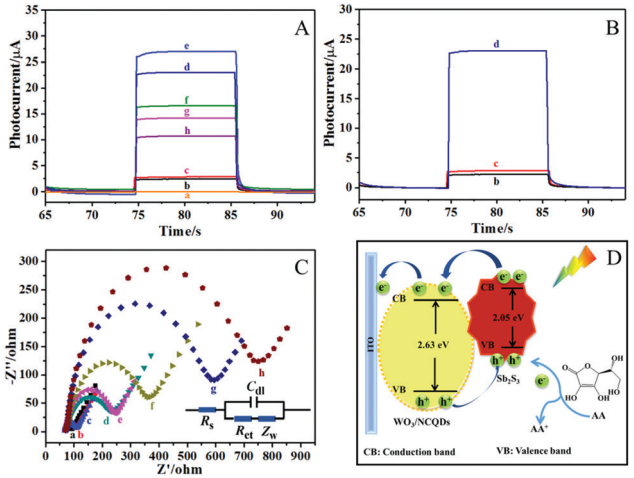

Fig. 3 (A and B) Photocurrent–time curves and (C) EIS Nyquist plots of (a) ITO, (b) ITO/WO_3, (c) ITO/WO_3/NCQDs, (d) ITO/WO_3/NCQDs/Sb_2S_3, (e) ITO/WO_3/NCQDs/Sb_2S_3/PDA, (f) ITO/WO_3/NCQDs/Sb_2S_3/PDA/anti-PCT, (g) ITO/WO_3/NCQDs/Sb_2S_3/PDA/anti-PCT/BSA, and (h) ITO/WO_3/NCQDs/Sb_2S_3/PDA/anti-PCT/BSA/PCT. The applied potential was 0 V (PCT = 0.1 ng mL^{-1}). (D) The electron transfer mechanism of the PEC immunosensor.

Combined with revised Fig. 2C (curve b), the sensitization of NCQDs could improve the absorption of WO_3 to visible light and the enhancement of photocatalytic performance.[45] It is worth mentioning that the photocurrent further increased from 3 μA to 24 μA with Sb_2S_3 modified on the surface of the NCQD-sensitized WO_3 (curve d). This is because the band gap edge of Sb_2S_3 was higher than that of WO_3, which led to the electron transfer from Sb_2S_3 to WO_3 promoted. However, the photocurrent was further increased to 27 μA (curve e) after PDA was modified onto the above composite. DA formed a PDA molecular membrane on the surface of the electrode through self-polymerization. In addition, the phenolic hydroxyl group on PDA had certain reducibility, which was beneficial to reducing photogenic holes, so as to achieve the purpose of separating photogenic electrons and photogenic holes. In this process, the photoelectron conduction was facilitated, so the photocurrent signals were enhanced. Subsequently, anti-PCT, BSA and PCT (0.1 ng mL^{-1}) were modified onto the electrode in sequence, the signal continually decrease (curve f, g and h), the layer-by-layer assembly of these proteins at the electrode blocked the transfer of electrons to the photoactive substrate, and partially masked the exciting light.[46] Furthermore, after the specific immune recognition, the photocurrent was significantly reduced. Therefore, the PEC immunosensor could be constructed for the detection of PCT.

The electrochemical impedance spectroscopy (EIS) Nyquist diagram (Fig. 3B) was used for further proving the successful construction of PEC immunosensors. The redox probe used was $[Fe(CN)_6]^{3-/4-}$ during this process. The inset in Fig. 3B shows that the resistance of solution (R_s), electron transfer resistance (R_{et}), double layer capacitance (C_{dl}) and Warburg impedance (Z_W) together compose the Randles equivalent circuit. The diameter of the semicircle revealed the value of R_{et}, which increased gradually with the sequential construction of PEC immunosensors. The uncoated ITO electrode showed a lower R_{et} (curve a) due to the low electron transfer resistance. In addition, an increase in semicircle diameter could be observed after modification with WO_3 (curve b). Subsequently, NCQDs (curve c) and Sb_2S_3 (curve d) were modified on the ITO/WO_3 electrode, and the impedances increased successively. When PDA was modified on the surface of Sb_2S_3, the R_{et} value increased slightly (curve e), which was because PDA as a polymer and its modification prevented the transference of electrons to the

electrode. Moreover, because the concentration of PDA was small and the polymerization time was relatively short, the thickness of the PDA film was not large, so the R_{et} value did not change much. Owing to insulation properties, the R_{et} values of the ITO/WO_3/NCQDs/Sb_2S_3/PDA electrode with the successive modification of anti-PCT, BSA and PCT (curve f, g and h) increased gradually. The results indicated that the PEC immunosensor could be put into use for the detection of PCT.

3.3. PEC mechanism of the immunoassay

Fig. 3C investigates the immunosensor about the electron transfer mechanism in AA electrolyte solution. The wide band gap (2.63 eV) of WO_3 (Fig. 2D) made the photo-generated electron/hole (e^-/h^+) formation difficult under the excitation of visible light. NCQDs has visible light absorption activity, which was conducive to improving the absorption of WO_3 to visible light and could enhance photocatalytic performance.[47] Therefore, NCQDs modified on WO_3 could enhance the PEC response. Moreover, Sb_2S_3 was a narrow band-gap semiconductor (Fig. S1C, ESI†) and had a good visible-light absorption activity. The perfect match between WO_3 and Sb_2S_3 energy level could induce photo-generated electron transfer efficiently from the conductive band of Sb_2S_3 to the conductive band of WO_3. Thus, the effective separation of e^-/h^+ pair was promoted, which led to generating high-intensity photoelectric signal. Therefore, the strong PEC response played a significant role in the successful construction of PEC immunosensors with high detection sensitivity.

3.4. Optimization of experimental conditions

PCT was detected with high sensitivity by optimizing the parameters (concentrations of $SbCl_3$ and AA, pH value) (Fig. S2, ESI†). As the concentration of $SbCl_3$ anhydrous ethanol solution increased, the photocurrent first increased and then decreased. The critical concentration was 0.06 mol L^{-1}, and the photocurrent rose to the highest value. Sb_2S_3 nanoparticles on the surface of WO_3 reached saturation at this critical concentration. Further increasing the concentration of $SbCl_3$ could cause excessive accumulation of Sb_2S_3, which could hinder electron transfer and make it difficult to absorb external light energy, leading to reduced photo-generated electron–hole generation rate. Therefore, the appropriate concentration of $SbCl_3$ solution was 0.06 mol L^{-1} (Fig. S2A, ESI†). AA, a great electron donor, impeded the recombination of the photo-generated e^-/h^+ pair to accelerate photo-generated carrier transmission. The concentration of AA was increasing and the photocurrent was also rising; when the concentration of AA was 0.15 mol L^{-1}, the photocurrent arrived at the optimum value. Besides, the visible light absorption of the WO_3/NCQDs/Sb_2S_3 composite was the strongest when the concentration of AA was optimum (Fig. S2B, ESI†). In addition, the photocurrent signal was strongest when the pH increased to 7.4. This indicated that the detection environment of the PBS buffer solution (pH 7.4) was similar to the physiological pH of human body, and also suitable for immobilizing protein activity. Therefore, in this experiment, we selected pH 7.4 buffer (PBS) for subsequent studies (Fig. S2C, ESI†).

3.5. PEC analysis for PCT

The ITO/WO_3/NCQDs/Sb_2S_3/PDA/anti-PCT/BSA electrodes were modified by various concentrations of PCT under optimal conditions. Fig. 4A and B reveals that the photocurrent decreased gradually as the concentration of PCT went up, which resulted from the insulating property of PCT. A linear decrease in photocurrent with the logarithm of PCT concentrations ranged from 0.001 ng mL^{-1} to 100 ng mL^{-1}, the linear equation was $I = 9.04 - 1.52 \log (c_{PCT}$, ng $mL^{-1})$, the correlation coefficient was 0.991, and the detection limit was 0.42 pg mL^{-1}.

The stability test of photocurrent response (PCT = 0.1 ng mL^{-1}) at 18 times on/off light cycles is shown in Fig. 4C. After a while, the photocurrent value had no distinct change, it showed the prepared PEC immunosensor had good stability. The relative standard deviation (RSD) was 1.8%, which was studied by five paralleled electrodes (10.01 μA, 9.61 μA, 9.49 μA, 10.12 μA and 9.83 μA) (Fig. S3, ESI†). Hence, the PEC immunosensor was accurate and reproducible.

Fig. 4D shows that the selective detection of PEC immunosensors for PCT detection. No obvious photocurrent change was discovered after 10 ng mL^{-1} of carcinoembryonic antigen (CEA), cardiac Troponin I (cTnI), and human immunoglobulin antigen (H-IgG) were modified on the blank electrode either mixed with PCT or not, respectively, which indicated that the PEC immunosensor had great selectivity and specificity for the determination of PCT.

3.6. Application of the PEC immunosensor in human serum

The accuracy and practicability of the PEC immunosensor was further examined by comparing the detection limit of PCT

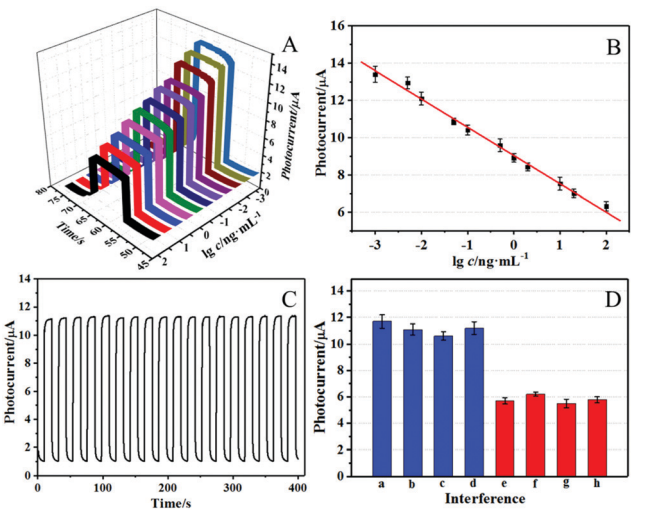

Fig. 4 (A) Photocurrent response curve under conditions of WO_3 (4.0 mg mL^{-1}), NCQDs (1 mol L^{-1}), $SbCl_3$ (0.06 mol L^{-1}), Na_2S (0.1 mol L^{-1}), and AA with 0.1 mol L^{-1} in pH 7.4 PBS buffer solution. (B) Logarithmic curve of the PEC immunosensor for PCT by different PCT concentrations. (C) The stability test of photocurrent response (PCT = 0.1 ng mL^{-1}) at 18 times on/off light cycles. (D) The selective detection of PEC immunosensor for PCT detection (a) blank, (b) blank + CEA (10 ng mL^{-1}), (c) blank + cTnI (10 ng mL^{-1}), (d) blank + H-IgG (10 ng mL^{-1}), (e) PCT (0.1 ng mL^{-1}), (f) PCT (0.1 ng mL^{-1}) + CEA (10 ng mL^{-1}), (g) PCT (0.1 ng mL^{-1}) + cTnI (10 ng mL^{-1}), and (h) PCT (0.1 ng mL^{-1}) + H-IgG (10 ng mL^{-1}). The applied potential was 0 V.

Table 1 Different detection methods for PCT

Method	Linear range (ng mL^{-1})	Detection limit (pg mL^{-1})	Ref.
PEC immunosensor	0.001–100	0.42	This method
Latex-enhanced immunoturbidimetric assay	0.16–56	260	48
Lateral flow immunoassay method	100–10 000	210	49
Capillary-based immunosensor	0.0025–80	0.5	50
Double antibody sandwich method	0.1–10	250	51
Homogeneous nanoparticle-based assay	0.016–100	18.6	52

Table 2 The testing results of PCT-spiked human blood serum samples

Content of PCT in serum sample	Added PCT concentration (ng mL^{-1})	The detection value (ng mL^{-1})	RSD (%, n = 5)	Recovery (%, n = 5)
0.09	0.50	0.63, 0.61, 0.55, 0.64, 0.54	4.62	100.8
	1.0	1.08, 1.05, 1.07, 1.06, 1.11	2.30	98.4
	5.0	5.08, 5.03, 5.11, 5.06, 5.13	3.96	99.8

under different detection methods (Table 1). By comparing different methods with this method, clearly, the method of PEC immunosensor used in this experiment had a wider detection range (0.001–100 ng mL^{-1}) and a lower detection limit (0.42 pg mL^{-1}). Moreover, the practicability of PEC immunosensors is revealed in Table 2, and the standard addition method was adopted to determine the PCT in human serum samples. The concentration of PCT in human serum was 0.09 ng mL^{-1}, the RSD value was 2.30–4.62%, and the recovery rate was 98.4–100.8%. The experimental results were satisfactory, indicating that the developed PEC immunosensor could excellently extend in practical detection. Combined with these satisfactory data, the PEC immunosensor has a potential application value in the field of biomolecular determination.

4. Conclusion

In summary, a novel PEC immunosensor with remarkable photoelectric performance was constructed for ultrasensitive detection of PCT utilizing NCQDs and Sb_2S_3 nanoparticle co-sensitized hydrangea-shaped WO_3 as a matrix. The three-dimensional structure of hydrangea endowed WO_3 a large surface area. NCQDs had a mass of carboxy groups and showed great PEC activities. After NCQDs and Sb_2S_3 nanoparticles co-sensitized hydrangea-shaped WO_3, the hydrangea-shaped WO_3/NCQDs/Sb_2S_3 composite was obtained and exhibited remarkable photoelectric properties. The excellent PEC response made the ultrasensitive detection of PCT possible. Moreover, the prepared PEC immunosensor processed wide detection range, high sensitivity, and low detection limit and showed high stability and selectivity for the detection of PCT. This novel and ultrasensitive PEC immunosensor had a broad application prospect in the fields of early diagnosis.

Conflicts of interest

There are no conflicts to declare.

Acknowledgements

This research was financially supported by the National Key Scientific Instrument and Equipment Development Project of China (No. 21627809), the National Natural Science Foundation of China (No. 21775053, 21575050, 21777056, 21505051), the Natural Science Foundation of Shandong Province (No. ZR2017MB027), the Jinan Scientific Research Leader Workshop Project (2018GXRC024).

References

1 R. Yang, K. Zou, X. Zhang, C. Du and J. Chen, *Biosens. Bioelectron.*, 2019, **132**, 55–61.
2 C. Tian, L. Wang, F. Luan, X. Fu, X. Zhuang and L. Chen, *Chem. Commun.*, 2019, **55**, 12479–12482.
3 H. Qi, B. Sun, J. Dong, L. Cui, T. Feng and S. Ai, *Sens. Actuators, B*, 2019, **285**, 42–48.
4 H. Li, X. He, H. J. Xiao, H. Du, J. Wang and H. Zhang, *Phys. Chem. Chem. Phys.*, 2017, **19**, 28056–28062.
5 T. Soltani, A. Tayyebi and B. K. Lee, *Appl. Surf. Sci.*, 2018, **448**, 465–473.
6 D. Fan, C. Bao, X. Liu, D. Wu, Y. Zhang, H. Wang, B. Du and Q. Wei, *J. Mater. Chem. B*, 2018, 7634–7642, DOI: 10.1039/c8tb02122h.
7 S. Zhang, X. Zhuang, D. Chen, F. Luan, T. He, C. Tian and L. Chen, *Mikrochim. Acta*, 2019, **186**, 450.
8 F. Luan, S. Zhang, D. Chen, K. Zheng and X. Zhuang, *Talanta*, 2018, **182**, 529–535.
9 F. H. You, M. Y. Zhu, L. J. Ding, Y. H. Xu and K. Wang, *Biosens. Bioelectron.*, 2019, **130**, 230–235.
10 P. E. A. Salomao, D. S. Gomes, E. J. C. Ferreira, F. Moura, L. L. Nascimento, A. O. T. Patrocinio and M. C. Pereira, *Sol. Energy Mater. Sol. Cells*, 2019, **194**, 276–284.
11 Z. Li, L. B. Yu, H. Song, L. Feng and X. P. Wang, *J. Mater. Sci.: Mater. Electron.*, 2018, **29**, 18059–18066.
12 B. Zhang, H. Wang, J. Xi, F. Zhao and B. Zeng, *Sens. Actuators, B*, 2019, **298**, 126835.

13 Y. Wang, F. Zhang, G. Zhao, Y. Zhao, Y. Ren, H. Zhang, L. Zhang, J. Du, Y. Han and D. J. Kang, *Ceram. Int.*, 2019, **45**, 7302–7308.
14 Z. Li, Y. Zhou, Q. Yao, W. Wang, H. Wang, D. Wang, X. Liu and J. Xu, *Mater. Lett.*, 2019, **236**, 197–200.
15 K. Sun, Q. Lu, C. Ma and M. Wei, *Mater. Lett.*, 2019, **236**, 267–270.
16 J. Chu, D. Lu, X. Wang, X. Wang and S. Xiong, *J. Alloys Compd.*, 2017, **702**, 568–572.
17 A. G. El-Shamy, *Mater. Sci. Semicond. Process.*, 2019, **100**, 245–254.
18 Y. Q. Geng, Z. Y. Xiang, C. Lv, Y. D. Wang, X. Xin and Y. Z. Yang, *Sep. Purif. Technol.*, 2019, **222**, 60–67.
19 D. Chen, X. Zhuang, J. Zhai, Y. Zheng, H. Lu and L. Chen, *Sens. Actuators, B*, 2018, **255**, 1500–1506.
20 J. S. Yang, H. X. Wu, P. Yang, C. J. Hou and D. Q. Huo, *Sens. Actuators, B*, 2018, **255**, 3179–3186.
21 C. H. Hua, H. C. Ma, X. L. Dong and X. F. Zhang, *Chem. Res. Chin. Univ.*, 2018, **39**, 200–205.
22 M. Lu and L. Zhou, *Mater. Sci. Eng., C*, 2019, **101**, 352–359.
23 V. Ramar, S. Moothattu and K. Balasubramanian, *Sol. Energy*, 2018, **169**, 120–127.
24 C. C. Xie, T. T. Fan, A. J. Wang and S. L. Chen, *Ind. Eng. Chem. Res.*, 2019, **58**, 120–127.
25 D. W. Fan, C. Z. Bao, X. Liu, D. Wu, Y. Zhang, H. Wang, B. Du and Q. Wei, *J. Mater. Chem. B*, 2018, **6**, 7634–7642.
26 J. Zhang, M. Yan, X. Z. Yuan, M. Y. Si, L. B. Jiang, Z. B. Wu, H. Wang and G. M. Zeng, *J. Colloid Interface Sci.*, 2018, **529**, 11–22.
27 P. Ganguly, S. Mathew, L. Clarizia, R. S. Kumar, A. Akande, S. Hinder, A. Breen and S. C. Pillai, *Appl. Catal., B*, 2019, **253**, 401–418.
28 Z. T. Ge, A. C. Yu and R. Lu, *Mater. Lett.*, 2019, **250**, 9–11.
29 D. Fan, X. Liu, C. Bao, J. Feng, H. Wang, H. Ma, D. Wu and Q. Wei, *Biosens. Bioelectron.*, 2019, **129**, 124–131.
30 D. Fan, C. Bao, X. Liu, J. Feng, D. Wu, H. Ma, H. Wang, Q. Wei and B. Du, *Talanta*, 2019, **198**, 417–423.
31 X. Sun, B. Li, C. Tian, F. Yu, N. Zhou, Y. Zhan and L. Chen, *Anal. Chim. Acta*, 2018, **1007**, 33–39.
32 W. Zhang, M. Tan, P. Zhang, L. Zhang, W. Dong, Q. Wang, J. Ma, E. Dong, S. Xu and G. Wang, *Appl. Surf. Sci.*, 2018, **455**, 1063–1069.
33 Y. Xu, W. Chen, L. Hu, X. Pan, S. Yang, Q. Shen and J. Zhu, *J. Alloys Compd.*, 2019, **784**, 947–953.
34 F. Li, L. Zhang, C. Hu, X. Xing, B. Yan, Y. Gao and L. Zhou, *Appl. Catal., B*, 2019, **240**, 132–140.
35 P. Seshadri, K. Manoli, N. Schneiderhan-Marra, U. Anthes, P. Wierzchowiec, K. Bonrad, C. Di Franco and L. Torsi, *Biosens. Bioelectron.*, 2018, **104**, 113–119.
36 Y. Li, W. Liu, G. Jin, Y. Niu, Y. Chen and M. Xie, *Anal. Chem.*, 2018, **90**, 8002–8010.
37 A. Rodríguez, L. F. Reyes, J. Monclou, B. Suberviola, M. Bodí, G. Sirgo, J. Solé-Violán, J. Guardiola, D. Barahona, E. Díaz, I. Martín-Loeches and M. I. Restrepo, *Med. Intensiva*, 2018, **42**, 399–408.
38 Y. Qian, J. Feng, H. Wang, D. Fan, N. Jiang, Q. Wei and H. Ju, *Sens. Actuators, B*, 2019, **300**, 127001.
39 T. Han, Y. Tao, Y. Li, C. Wei, X. Pang, Q. Huang and W. Qin, *Carbon*, 2015, **91**, 144–152.
40 M. Alimoradi and M. Adelifard, *J. Anal. Appl. Pyrolysis*, 2019, **140**, 205–212.
41 P. Salinas-Estevane and E. M. Sánchez, *Cryst. Growth Des.*, 2010, **10**, 3917–3924.
42 P. Zhou, Y. Shen, S. Zhao, G. Li, Y. Yin, R. Lu, S. Gao, C. Han and D. Wei, *J. Alloys Compd.*, 2019, **789**, 129–138.
43 H. P. Chauhan, J. Carpenter and S. Joshi, *Spectrochim. Acta, Part A*, 2014, **130**, 230–237.
44 Q. J. Cai, Z. F. Liu, C. C. Han, Z. F. Tong and C. H. Ma, *J. Alloys Compd.*, 2019, **795**, 319–326.
45 X. Miao, X. Yue, Z. Ji, X. Shen, H. Zhou, M. Liu, K. Xu, J. Zhu, G. Zhu, L. Kong and S. A. Shah, *Appl. Catal., B*, 2018, **227**, 459–469.
46 W. W. Zhao, Z. Y. Ma, P. P. Yu, X. Y. Dong, J. J. Xu and H. Y. Chen, *Anal. Chem.*, 2012, **84**, 917–923.
47 X. Pang, Y. Zhang, J. Pan, Y. Zhao, Y. Chen, X. Ren, H. Ma, Q. Wei and B. Du, *Biosens. Bioelectron.*, 2016, **77**, 330–338.
48 M. Dipalo, R. Buonocore, C. Gnocchi, A. Picanza, R. Aloe and G. Lippi, *Clin. Chem. Lab. Med.*, 2015, **53**, 593–597.
49 A. S. Ghrera, *Anal. Chim. Acta*, 2019, **1056**, 26–33.
50 R. B. Nie, X. X. Xu, X. J. Cui, Y. P. Chen and L. Yang, *ACS Omega*, 2019, **4**, 6210–6217.
51 Y. Zhou, X. M. Shao, Y. W. Han and H. M. Zhang, *Anal. Methods*, 2018, **10**, 1015–1022.
52 P. Li, Z. H. Chen, B. Liu, K. Li, H. Wang, L. Lin, L. He, J. Wei and T. C. Liu, *Int. J. Nanomed.*, 2018, **13**, 5395–5404.

